

Atmospheric Aerosol Optical Properties
in the Persian Gulf Region

Alexander Smirnov

Science Systems and Applications, Inc, and NASA Goddard Space Flight Center, Greenbelt, MD

Brent N.Holben

Biospheric Sciences Branch, NASA Goddard Space Flight Center, Greenbelt, MD

Oleg Dubovik

Science Systems and Applications, Inc, and NASA Goddard Space Flight Center, Greenbelt, MD

Norm T.O'Neill

Centre d'applications et de recherches en teledetection, Universite de Sherbrooke, Sherbrooke,

Quebec, Canada

Thomas F.Eck

Goddard Environmental Science and Technology Center, University of Maryland Baltimore

County, and NASA Goddard Space Flight Center, Greenbelt, MD

Douglas L.Westphal and Andreas K.Goroch

Naval Research Laboratory, Monterey, CA

Christophe Pietras

General Sciences Corporation, Beltsville, MD

Ilya Slutsker

Science Systems and Applications, Inc, and NASA Goddard Space Flight Center, Greenbelt, MD

Submitted to the Special issue of Journal of the Atmospheric Sciences, January 30, 2001.

Corresponding Author: Alexander Smirnov, code 923, NASA/ Goddard Space Flight Center,

Greenbelt, MD 20771; Tel.: (301)-614-6626; Fax: (301)-614-6695; E-mail:

asmirnov@aeronet.gsfc.nasa.gov

ABSTRACT

Aerosol optical depth measurements over Bahrain acquired through the ground-based Aerosol Robotic Network are analyzed. Optical depths obtained from ground-based sun/sky radiometers showed a pronounced temporal trend, with a maximum dust aerosol loading observed during the March to July period. The aerosol optical depth probability distribution is rather narrow with a modal value of about 0.25. The Angstrom parameter frequency distribution has two peaks. One peak around 0.7 characterizes a situation when dust aerosol is more dominant, the second peak around 1.2 corresponds to relatively dust-free cases. The correlation between aerosol optical depth and water vapor content in the total atmospheric column is strong (correlation coefficient of 0.82) when dust aerosol is almost absent (Angstrom parameter is greater than 0.7), suggesting possible hygroscopic growth of fine mode particles or source region correlation, and much weaker (correlation coefficient of 0.45) in the presence of dust (Angstrom parameter is less than 0.7). Diurnal variations of the aerosol optical depth and precipitable water were insignificant. Angstrom parameter diurnal variability (~20-25%) is evident during the April-May period, when dust dominated the atmospheric optical conditions. Variations in the aerosol volume size distributions retrieved from spectral sun and sky radiance data are mainly associated with the changes in the concentration of the coarse aerosol fraction (variation coefficient of 61%). Geometric mean radii for the fine and coarse aerosol fractions are 0.14 μm (s.d.=0.02) and 2.57

μm (s.d.=0.27), respectively. The geometric standard deviation of each fraction is 0.41 and 0.73 respectively. In dust-free conditions the single-scattering albedo (SSA) decreases with wavelength, while in the presence of dust the SSA either stays neutral or increases slightly with wavelength. The changes in the Angstrom parameter derived from ground-based nephelometer and co-located sunphotometer during the initial checkout period were quite similar.

1. Introduction

Remotely measured atmospheric aerosol optical parameters are important for various applications including computations of radiative forcing and satellite remote sensing. Aerosol optical depth, which may be derived from measurements of attenuated direct solar radiation, as well as the aerosol size distribution and single-scattering albedo, which may be derived from combined aerosol optical depth and solar almucantar sky radiance data, are pivotal parameters defining the aerosol optical state of the atmosphere (King et al. 1999; Kaufman et al. 1997). The major advantage of these kind of remote sensing measurements over direct in-situ aerosol sampling or laboratory analysis is their large-scale (column integrated quantities) and non-intrusive nature. Satellite based remote sensing methods along with the ground-based methods have produced promising results (Kaufman et al. 2000; Tanre et al. 2001).

Mineral dust, considered as a part of the natural background aerosol, often has been neglected in anthropogenic climate change considerations (Andreae 1996). Although it is not presently possible to adequately characterize the influence of mineral dust on global climate, Li et al. (1996) suggest that it could be an important climate-forcing component over specific oceanic areas and other regions where dust concentration is high. Dust plays an important role in radiative processes and its optical properties are important for various estimations of radiative forcing (Miller and Tegen 1998).

Despite the long history of dust aerosol studies our knowledge of dust optical properties is still far from being sufficient (Sokolik and Toon 1999). Dust composition plays an important role in determining these optical properties and a priori knowledge of the real variability of aerosol optical parameters over different areas is of interest for many studies. One cannot generalize dust optical properties to a global scale despite observations such as those of Prospero (1999) that dust collected in the western Atlantic had similar mineral composition to dust collected off the coast of Africa. Sokolik and Toon (1999) have shown that aerosol extinction, single-scattering albedo and the phase function asymmetry parameter are very sensitive to the individual minerals and their mixtures in dust composition.

Aerosol optical properties have not been well studied in the Persian Gulf region. Characteristics of desert aerosols in the Persian Gulf area were derived from the Landsat data by Otterman et al. (1982). Ground-based or airborne data were acquired mainly in the spring or summer of 1991 (see e.g. Hobbs and Radke (1992), Nakajima et al (1996)) and were focused on the smoke from the Kuwait oil fires. The 14 months record of the Linke turbidity factor in Bahrain (Alnaser and Awadalla 1995) was also influenced by aerosol from oil fires.

In the current study we analyze atmospheric aerosol optical properties over Bahrain, investigate seasonal variability of aerosol optical depth and its spectral behavior, establish a relationship between optical depth and precipitable water, and present volume size distribution and single-scattering albedo dynamics.

2. Instrumentation, data collection and synoptic air mass characterization

An automatic Sun and sky scanning radiometer CIMEL was established as an Aerosol Robotic Network (AERONET) site in Bahrain (latitude $26^{\circ}16' N$, longitude $50^{\circ}39' E$) in July 1998 (Figure 1). The instrument deployed was a re-engineered CIMEL radiometer belonging to the SIMBIOS project (McClain and Fargion 1999). The re-engineering included a number of modifications to “harden” the sun/sky radiometer for deployments in marine environments. The instrument was located on the grounds of the US Naval Central Meteorology and Oceanography Facility at Bahrain, approximately 7 km from the Bahrain International Airport. The sun/sky radiometer was mounted on top of a standard trailer, approximately 3.2 m above ground, with no obstructions to the sun above 10 degrees elevation. The CIMEL radiometer made measurements of the direct sun and diffuse sky radiances within the spectral range 340-1020 nm and 440-1020 nm respectively (Holben et al. 1998). The direct sun measurements are acquired in eight spectral channels at 340, 380, 440, 500, 675, 870, 940 and 1020 nm (nominal wavelengths). Seven of the eight bands are used to acquire aerosol optical depth data. The eighth band at 940 nm is used to estimate total precipitable water content. The bandwidths of the ion-assisted deposition interference filters employed in the CIMEL radiometer vary from 2-4 nm (UV channels) to 10 nm for visible and near infrared channels. The ratio of transmittance in the center of the band to the transmittance in the wings is higher than 10^4 , thus minimizing out-of-band leakage. The

silicon photodiode, used as a detector, is not temperature stabilized but its temperature is routinely monitored and a correction is systematically applied to the 1020 nm channel voltages as recommended by the manufacturer and verified and quantified by laboratory temperature testing.

Holben et al. (1998) and Eck et al. (1999) presented careful assessments of the overall uncertainty in computed τ_a due to calibration uncertainty and lack of both surface pressure data and actual ozone column amount. Typically, the total uncertainty in $\tau_a(\lambda)$ for a field instrument is $\sim\pm 0.01$ to ± 0.02 , and is spectrally dependent with the higher errors in the UV spectral range.

Schmid et al. (1999) showed that discrepancies between aerosol optical depths measured by a CIMEL radiometer and four other radiometers in field experimental conditions were within 0.015 (rms). The details of the water vapor content retrieval procedure and the types of errors involved can be found in Schmid et al. (2000). The extracted water vapor content in the total atmospheric column (in cm of precipitable water) is usually consistent to within $\sim 10\%$ of radiosonde or microwave radiometer measurements.

The sky radiance almucantar measurements are acquired in four spectral channels at 440, 670, 870 and 1020 nm. For each solar zenith angle sky radiances are taken at 28 azimuth angles within the relative azimuth angle range (from the Sun) of $2-180^\circ$ (Holben et al. 1998). A flexible inversion algorithm for retrieval of aerosol optical properties, developed by Dubovik and King (2000), was used for retrieving aerosol volume size distributions over a range of sizes from 0.05-

15 μm together with spectrally dependent complex refractive index and single scattering albedos from spectral sun and sky radiance data. This approach is significantly different from earlier studies in that simultaneous retrieval of the particle size distribution and complex refractive index via fitting of radiances measured in the entire available angular and spectral range was implemented. The optimized inversion algorithm was built on the principles of statistical estimation: the spectral radiances and various a priori constraints on aerosol characteristics were considered as multi-source data that were known with predetermined accuracy. The inversion was designed as a search for the best fit of all input data by a theoretical model that takes into account the different levels of accuracy of the fitted data. An inversion strategy, details of the algorithm development and the methodological aspects of the detailed statistical optimization of the influence of noise in the inversion procedure are discussed in depth in (Dubovik and King 2000).

The accuracy of the aerosol particle size distributions and single scattering albedos has been studied in detail by Dubovik et al. (2000). Retrieval errors in $dV/d\ln R$ typically do not exceed 15-35% (depending on aerosol type) for each particle radius bin within the 0.1-7 μm range. The errors for very small particles ($r \sim 0.05$ -0.1 μm) and very large particles ($r \sim 7$ -15 μm) may be as large as 35-100% (for each particle radius bin). However, no significant shifts in the positions of mode radii or changes in the shape of size distributions are expected. Single scattering albedos

(SSA) are expected to have an uncertainty of 0.03-0.05 depending on aerosol type and loading (Dubovik et al. 2000).

An automatized and computerized cloud screening algorithm (Smirnov et al. 2000) was applied to the direct sun measurements. Because of the fairly low cloud fraction throughout the measurement period approximately 80% of the original data remained after the application of the complete screening procedure.

Bahrain is situated on the western side of the Persian Gulf between Saudi Arabia and Qatar. The Persian Gulf itself extends from the Euphrates River delta to the Strait of Hormuz. According to the Forecaster's Handbook (Heishman 1999) the area's long-term climatology has enabled the following seasonal divisions to be established for the Persian Gulf: southwest monsoon (June-September), fall transition (October-November), northeast monsoon (December-March), and spring transition (April-May). During the southwest monsoon a northwesterly flow occurs at all levels over the Arabian Peninsula bringing extremely dry air and dust from the Iraqi deserts. During the fall transition season, winds remain northwesterly but speeds decrease, the frequency of occurrences of dust storms decreases significantly, and air temperatures drop. The northeast monsoon is characterized by a very complex airflow pattern, which can be a combination of land-sea breezes, outflow from the Persian Gulf and northeasterly flow off the Iranian coast. Dust usually is advected from Saudi Arabia, Iraq or southern Iran (Liu et al. 2000). In the April-May period winds are predominantly from the North or North-northwest, and the

frequency of dust storms increases. The analyzed measurement period of one year was influenced by all the seasonal dynamics described above.

3. Results

3.1. Intra-annual variability of optical parameters and water vapor content

For simplicity we will characterize atmospheric aerosol optical conditions by two parameters: $\tau_a(500 \text{ nm})$, which is the aerosol optical depth at a wavelength of 500 nm, and the Angstrom parameter α derived from a multi-spectral log linear fit to the classical equation $\tau_a \sim \lambda^{-\alpha}$ (based on four wavelengths in the range 440-870 nm). Although not all optical depth spectra are well represented by an Angstrom fit (see, e.g., (King and Byrne 1976; Kaufman 1993; Villevalde et al. 1994; Eck et al. 1999; O'Neill et al. 2001)), the Angstrom parameter α can still be considered as a first-order indicator of average spectral behavior. It is noted that for bimodal size distributions and coarse mode dominated size distributions (both of which frequently occur in Bahrain) the spectral curvature of $\ln\tau_a$ versus $\ln\lambda$ is very small (Eck et al. 1999).

Figure 2a illustrates the monthly averaged aerosol optical depth at 500 nm for the one year record (July 1998-July 1999) in Bahrain. A total of 324 daily averages contributed to the statistics of this figure. The monthly mean aerosol optical depth increases by about 50% from the June value to a peak in July and August and decreases back to below the June value by October.

The mean of $\tau_a(500 \text{ nm})$ in July 1999 is 0.49. In contrast, the mean aerosol optical depth

between the months of October and January decreases to a minimum of about ~ 0.21 in December. Standard deviations generally increase with the mean values of τ_a . Monthly averages of the Angstrom parameter α for the whole period of observations are shown in Figure 2b. The notable decrease of the Angstrom parameter α (Figure 2b) during the March-July 1999 period is associated with the presence of dust in the aerosol loading. The mean monthly values of the Angstrom parameter show a general trend characterized by a November-December maximum and a late spring and early summer minimum. The mean monthly values of α vary within the 0.4-1.3 range. Mean monthly values of the water vapor content (WVC) are, generally, around 2 cm of precipitable water except for the months of July through September 1998 when they stay above 3 cm (Figure 2c).

The daily average values of τ_a (500 nm) for the measurement period do show very large day to day variations (Figure 3a). The annual pattern with an increase to maximal turbidity in the April-September period is apparent. These observations indicate that the optical depth at 500 nm very rarely exceeds 0.7. The October-January minimum is also in evidence and daily average τ_a (500 nm) drops below 0.1 on a few occasions in this period. High daily average values of the Angstrom parameter α from August 1998 to February 1999 reflect the presence of a significant fraction of fine particles in the aerosol size distribution. The origin of this aerosol is, most likely, local or regional anthropogenic pollutants. Dusty conditions prevailed starting in March and α remained below unity until the end of the analyzed period. The daily average values of the total

precipitable water amount (or water vapor content in cm) (Figure 3c), show higher values of 2 to 5 cm in the summertime, while in October-May values are less than 3 cm. This is consistent with the general synoptic pattern for the region.

Frequency histograms of τ_a , α and WVC are shown in Figures 4a-4c for the daily averaged data. The aerosol optical depth probability distribution is rather narrow with a modal value of about 0.25. The probability distribution of α is relatively broader with two modal values of about 0.7 and 1.1-1.3. The frequency histogram of WVC shows a maximum at 1.75 cm.

Histograms of the τ_a , α and WVC values categorized by season are presented in Figure 5. For the June-September season we combined the data from July-September 1998 and June-July 1999. The October-November season has the narrowest τ_a probability distribution with a modal value of 0.25. The distribution in the December-March season is wider and the maximum is spread around $\tau_a \sim 0.20$. The rest of the year can be characterized by a significant increase in the τ_a modal value (0.35), which we ascribe to the presence of dust aerosol. A parallel set of graphs of the Angstrom parameter displays an obvious seasonal trend. In October-November the α distribution is narrow and peaks around $\alpha \sim 1.5$. In the April-May season dusty conditions prevail and the maximum of the distribution shifts towards smaller α near 0.7. The broad June-September and December-March distributions characterize complex conditions, when dust is also present; however, non-dust conditions occur relatively more often. The total column integrated water vapor amounts also show significant seasonal variability. The distribution is

wider in June-September, while the October-November and April-May distributions have similar narrower forms (modal value of WVC \sim 2.25 cm).

The scattergram of daily averages of aerosol optical depth versus Angstrom parameter is shown in Figure 6a. This optical representation often allows one to define physically interpretable cluster regions for different types of aerosols. Although no obvious cluster discrimination is evident in Figure 6a, one feature is worth noting: a wide range of α at moderate to low aerosol optical depths (<0.6). The relationship between daily averages of water vapor content and aerosol optical depth at 500 nm (Figure 6b) shows notable correlation (correlation coefficient of 0.61). This result is evident in the annual variability trends of τ_a and WVC of Figures 3a and 3c. For the whole data set a linear fit explained 37% of the variance:

$$\tau_a (500 \text{ nm}) = 0.101\text{WVC} + 0.095,$$

where WVC is the water vapor content in the total atmospheric column (in centimeters of precipitable water). If we divide our data set into dusty ($\alpha < 0.7$, gridded squares in Figure 6b) and dust-free classes ($\alpha > 0.7$, solid circles in Figure 6b), then the correlation coefficients are computed to be of 0.45 and 0.82 respectively and regression relationships are found to be as follows:

$$\tau_a (500 \text{ nm}) = 0.097\text{WVC} + 0.192, \text{ (for } \alpha < 0.7),$$

$$\tau_a (500 \text{ nm}) = 0.115\text{WVC} + 0.024, \text{ (for } \alpha > 0.7).$$

The scatter plot of α versus WVC (Figure 6c) does not yield any distinguishable pattern.

3.2. Diurnal variability of optical parameters and water vapor content

For various applications the diurnal variability of atmospheric optical parameters and precipitable water is of great importance. Also, the hourly statistics themselves are of interest for atmospheric correction and validation efforts. Using our data set we computed the diurnal τ_a (500 nm), α and WVC variations according to the following procedure. All individual observations for a day are expressed as a percentage departure from the daily mean. Computed percentages were averaged over each hour (0300-0400 GMT, 0400-0500 GMT etc.) for each month and season (June-September, October-November, December-March, and April-May). This sampling procedure which is similar to one used by Peterson et al. (1981) renders systematic diurnal trends more evident.

The seasonal results are shown in Figure 7 (local noon comes at ~0830 GMT). Each hourly average consists of at least several dozen individual observations. Diurnal variations of precipitable water are similar for all the seasons and practically insignificant (plus or minus a few percent from the daily averages). The diurnal variation of the Angstrom parameter (computed from linear regression of 440, 500, 675, and 870 nm data) is most pronounced in the April-May season, however, this is the dust season when α is smaller thus a similar $\Delta\alpha$ will result in a higher percentage difference than for high α months. A diurnal cycle of local pollutants (fine mode aerosols) may be responsible for this slight increase of the Angstrom parameter. Consideration of the short wavelength (380 and 500 nm) Angstrom exponent, which

is more sensitive to the fine mode aerosol variations (Reid et al. 1999), frequently shows a diurnal pattern with the maximum around or after midday. In the April-May season the presence of dust masks the diurnal pattern in optical depth. In the October-November period local and /or regional pollutants along with atmospheric convection played a major role in the slight diurnal increase of the optical depth.

Certain peculiarities can be seen in Figure 8, which presents computed hourly statistics for each season. The hourly statistics can be biased if the number of measurements considered within averaging periods is significantly different. Thus, diurnal variability (in the sense of the hourly averages) can be different from established percent departure from daily averages. Figure 8 shows a notable diurnal cycle for the Angstrom parameter during the June-September and April-May seasons. Figure 8 indicates no variability of the aerosol optical depth. Water vapor content variation is noticeable only in June-September season (Figure 8).

Figures 7 and 8 demonstrate diurnal dynamics of the aerosol optical depth, Angstrom parameter and water vapor content. This results are generally consistent with the analysis of Kaufman et al. (2000), where data from ~70 AERONET sites over 7 years showed that late morning (1000-1130 LST) or early afternoon (1230-1400 LST) averages represent the entire daily average values within 5%.

3.3. Volume size distribution and single scattering albedo retrievals

Aerosol optical properties (aerosol volume size distributions and single scattering albedos) were retrieved from spectral sun and sky radiance data by an iterative algorithm (Dubovik and King 2000) with the following initial guess: $dV/d\ln R=0.0001$, $n(\lambda_i)=1.50$, $k(\lambda_i)=0.005$, where $dV/d\ln R$ denotes aerosol volume size distribution, $n(\lambda_i)$ and $k(\lambda_i)$ denote real and imaginary parts of the refractive index at a wavelength λ_i . The inversion algorithm produces retrievals, which correspond to the effective optical properties for the total atmospheric column. In the retrieval algorithm the aerosol particles are assumed to be polydisperse homogeneous spheres.

Dubovik et al. (2000) showed that the size distribution, in the case of non-spherical dust aerosols can be retrieved reasonably well when the angular range of sky radiances is limited to scattering angles smaller than 30-40°. However, in order to retrieve the single scattering albedo the sky radiances acquired in the whole almucantar are needed along with the direct sun measurements. Thus for non-spherical dust aerosols, we should use the early morning or late afternoon (scattering angle range is large) sky radiance measurements to retrieve a single scattering albedo and sky radiances acquired around midday (scattering angle range is small) to extract aerosol size distributions (Dubovik et al. 2000).

Figures 9 and 10 illustrate seasonal and monthly averaged size distributions ($dV/d\ln R$). The dominant variations in these distributions can be directly associated with significant changes in the amplitude and spectral dependence of the optical depth data. The fine mode shows relative stability, while the coarse fraction changes significantly. Separate averaged size distributions for

April and May have been plotted in Figure 9 in order to show the aerosol dynamics during this particular spring transition season. The variation of the magnitude and shape of the coarse aerosol fraction between March and September is attributed to incoming dust (Figure 10). The fine aerosol fraction changed as well, but there were no significant changes in the magnitude and shape of size distributions, except for the month of May. The fine mode geometric mean radius in May was smaller. Perhaps this is an artifact of non-sphericity in our retrieval algorithm, which may appear when desert dust aerosol dominates (Dubovik et al. 2000).

Table 1 presents parameters of the bi-modal lognormal volume size distributions (Whitby, 1978; Remer et al. 1999) shown in Figures 9 and 10. For each mode the lognormal distribution is defined as:

$$\frac{dV}{d\ln R} = \frac{C_v}{\sigma\sqrt{2\pi}} \exp\left(-\frac{1}{2} \left(\frac{\ln(R/R_v)}{\sigma}\right)^2\right),$$

where $dV/d\ln R$ is the volume distribution, the volume concentration C_v is the columnar volume of particles per unit cross section of atmospheric column, R is the particle radius, R_v is the volume geometric mean radius, σ is the geometric standard deviation. Effective radius is defined as a ratio of the third over the second moment of the number size distribution. It should be noted that we assigned particles with radii $0.05 < r < 0.3-0.6 \mu\text{m}$ and with radii $0.3-0.6 < r < 15 \mu\text{m}$ to the fine and coarse modes respectively (before and after the inflection point). Volume concentrations for each fraction are also presented in Table 1.

Variations in aerosol volume size distributions over Bahrain were largely due to changes in the concentration of the coarse aerosol fraction (variation coefficient, defined as standard deviation divided by average, of 61%). The annual averaged particle fine and coarse mode geometric mean radii were $0.14 \mu\text{m}$ (s.d.=0.02) and $2.57 \mu\text{m}$ (s.d.=0.27), respectively. Variation coefficients yielded values of 15% for the fine mode R_V and 24% for the fine mode σ , and 10% and 8% for the coarse mode parameters (Table 1).

Single scattering albedos (SSA) are shown in Figure 11. The vertical bars indicate plus or minus one standard deviation. Two major features of the SSA spectral dependence can be observed. When dust is not the major contributor to the atmospheric optical state the SSA has a selective spectral dependence (SSA decreases with wavelength). The values and spectral dependence of the SSA from August till March systematically show this type of spectral dependence. In the presence of dust the spectral dependence of the SSA is almost neutral (in May the SSA even increases slightly with the wavelength) and values are higher because dust absorbs less than the anthropogenically influenced aerosol. An increase of single scattering albedo with wavelength can be caused by the domination of coarse particle mode (dust in our case) in the aerosol size distribution (e.g., (Ackerman and Toon 1981)) and by higher absorption in the blue spectral band (Kaufman et al. 2001). Levin et al. (1980) reported low absorption of the dust aerosol in the center of the visible spectral range. For the Persian Gulf region dust

aerosols Otterman et al. (1982) reported very weak absorption within the 500-1100 nm spectral range. Our results are consistent with this finding.

3.4. Comparison of Angstrom parameters derived from a nephelometer and the sunphotometer

The sunphotometer data were compared to surface nephelometer measurements during the initial checkout period immediately after instrument installation. The nephelometer was a TSI (TSI Model 3650) three wavelength integrating nephelometer (Anderson et al. 1996). The instrument was located inside an air-conditioned trailer with an outside sampling tube consisting of 3 m of 5 cm (2 in) inside diameter clear plastic tubing. The sampling chamber was heated $\sim 3^{\circ}\text{C}$ to minimize condensation problems. The data were acquired on a portable computer with an averaging time of 5 minutes. The system collected scattering coefficients integrated over the total sphere (7-170 degrees) as well as over the back hemisphere (90-170 degrees) at blue, green and red wavelengths (450, 550, and 700 nm). Only the total hemisphere scattering coefficients were used in the analysis we present here.

The total scattering from the sample at three wavelengths was used to calculate the Angstrom parameter derived from a multi-spectral log linear fit. The sunphotometer and nephelometer were compared over a three day period from July 23 to July 25, 1998. Figure 12 shows that the Angstrom parameters computed from the sunphotometer and nephelometer were similar. This level of agreement indicates that the aerosol size distribution in the local sampling volume of the

nephelometer and the size distribution in the vertical column were similar in form. During the day when optical depth measurements were available, the coefficients were similar in the range from 0.4 on July 23 to 1.1 on July 25, suggesting similar aerosol size distributions at the surface and in the total column. At night and into next morning, the nephelometer Angstrom parameter showed a strong increase, indicating that the relative proportion of large particles decreased substantially during the night, while the sunphotometer α was still low the following morning. Thus on the morning of July 26, the data suggest that there were significantly more large particles (dust) aloft than at the surface where fine mode aerosol dominated.

4. Conclusions

The principal conclusions drawn from our work can be summarized as follows:

1. It was found that intra-annual variability of the optical properties (aerosol optical depth and Angstrom parameter) over Bahrain was significant for the time period of this study. Seasonal and diurnal variations of optical parameters showed that the dust aerosol concentrations were a major contributor to optical depth and Angstrom parameter variability. The limitations of the data set size (~1 year) preclude the establishment of definitive aerosol climatology for this region.
2. Regression relationships between aerosol optical depth and water vapor content in the total atmospheric column have been derived for relatively dust-free conditions as well as for dusty conditions. If another criterion to choose between dust-free and dust loaded conditions is

available (such as a threshold on α) then these relationships, in particular for relatively dust free cases, can be used to predict optical depth from values of precipitable water.

3. Optical inversions of sky radiance and optical depth data indicate that the variations in aerosol volume size distributions over Bahrain were largely due to changes in the concentration of the coarse aerosol fraction (variation coefficient of 61%).

4. The spectral variability of the single-scattering albedo was different during the dusty and non-dusty conditions. In the presence of dust the spectral dependence of the SSA was almost neutral.

When dust was not a major component, the SSA decreased with wavelength. This decreasing spectral trend is similar to results obtained for urban pollution and smoke aerosols (Dubovik et al. 2001).

5. The changes in the Angstrom parameter α derived from a ground-based nephelometer and a co-located sunphotometer were quite similar over the July 23 and July 25 time period, when both observed a modest increase. The agreement implies a degree of vertical homogeneity in the aerosol distribution during the period when the two instruments were co-located.

Acknowledgments. The authors thank Dr. Robert Curran of NASA Headquarters and Dr. Michael King of the EOS Project Science Office for their support. The support of the Office of Naval Research and Naval Research Laboratory through programs PE-0602435N and PE-06-1153 is gratefully acknowledged. The authors would like to thank R.Fraser and R.Ferek for fruitful discussions of certain issues. The authors would also like to acknowledge the constructive criticism of anonymous reviewers.

REFERENCES

- Ackerman, P., and O.B.Toon, 1981: Absorption of visible radiation in atmosphere containing mixtures of absorbing and nonabsorbing particles, *Appl.Opt.*, **20**, 3661-3668.
- Alnaser, W.E., and N.S.Awadalla, The Linke turbidity factor and Angstrom coefficient in humid climate of Bahrain, 1995: *Earth, Moon and Planets*, **70**, 61-74.
- Anderson, T.L., et al., 1996: Performance characteristics of a high sensitivity three-wavelength total scatter/backscatter nephelometer, *J.Atmos.Ocean.Technol.*, **13**, 967-986.
- Andreae, M.O., 1996: Raising dust in the greenhouse, *Nature*, *380*, 389-390.
- Dubovik, O., B.N.Holben, T.F.Eck, A.Smirnov, Y.J.Kaufman, M.D.King, D.Tanré, and I.Slutsker, 2001: Variability of absorption and optical properties of key aerosol types observed in worldwide locations, *J. Atm. Sci.*, (submitted).
- Dubovik, O., and M.D.King, 2000: A flexible inversion algorithm for retrieval of aerosol optical properties from sun and sky radiance measurements, *J.Geophys.Res.*, **105**, 20,673-20,696.
- Dubovik, O., A.Smirnov, B.N.Holben, M.D.King, Y.J.Kaufman, T.F.Eck, and I.Slutsker, 2000: Accuracy assessments of aerosol optical properties retrieved from AERONET sun and sky radiance measurements, *J.Geophys.Res.*, **105**, 9791-9806.
- Eck, T.F., B.N.Holben, J.S.Reid, O.Dubovik, A.Smirnov, N.T.O'Neill, I.Slutsker and S.Kinne, 1999: Wavelength dependence of the optical depth of biomass burning, urban, and desert dust aerosol, *J.Geophys.Res.*, **104**, 31,333-31,350.

Heishman, J., Commanding Officer, 1999: US Navy Central Meteorological and Oceanographic Center, Bahrain, personal communication.

Hobbs, P.V., and L.W.Radke, 1992: Airborne studies of the smoke from the Kuwait oil fires, *Science*, **256**, 987-991.

Holben, B.N., T.F.Eck, I.Slutsker, D.Tanre, J.P.Buis, A.Setzer, E.Vermote, J.A.Reagan, Y.J.Kaufman, T.Nakajima, F.Lavenu, I.Jankowiak, and A.Smirnov, 1998: AERONET - A federated instrument network and data archive for aerosol characterization, *Rem.Sens.Env.*, **66(1)**, 1-16.

Iqbal, M., 1983: *An Introduction to Solar Radiation*, 390 p.p., Academic, San Diego, Calif.

Kaufman, Y.J., D.Tanre, O.Dubovik, A.Karnieli, and L.A.Remer, 2001: Satellite and ground based radiometers reveal much lower dust absorption of sunlight than used in climate models, *Geophys. Res. Let.*, (accepted, in press).

Kaufman, Y.J., B.N.Holben, D.Tanre, I.Slutsker, T.F.Eck, A.Smirnov, 2000: Well aerosol measurements from Terra and Aqua polar orbiting satellites represent the daily aerosol abundance and properties? *Geophys. Res. Let.*, **27**, 3861-3864.

Kaufman, Y.J., D.Tanre, H.R.Gordon, T.Nakajima, J.Lenoble, R.Frouin, H.Grassl, B.M.Herman, M.D.King, and P.M.Teillet, 1997: Passive remote sensing of tropospheric aerosol and atmospheric correction for the aerosol effect, *J.Geophys.Res.*, **102**, 16,815-16,830.

Kaufman, Y.J., 1993: Aerosol optical thickness and atmospheric path radiance, *J.Geophys.Res.*, **98**, 2677-2692.

King, M.D., Y.J.Kaufman, D.Tanre, and T.Nakajima, 1999: Remote sensing of tropospheric aerosols from space: Past present and future, *Bull.Amer.Meteor.Soc.*, **80**, 2229-2259.

King, M.D., and D.M.Byrne, 1976: A method for inferring total ozone content from spectral variation of total optical depth obtained with a solar radiometer, *J.Atmos.Sci.*, **33**, 2242-2251.

Levin, Z., J.H.Joseph, and Y.Mekler, 1980: Properties of Sharav (Khamsin) dust - comparison of optical and direct sampling data, *J.Atmos.Sci.*, **37**, 882-891.

Li, X., H.Maring, D.Savoie, K.Voss, and J.M.Prospero, 1996: Dominance of mineral dust in aerosol light-scattering in the North Atlantic trade winds, *Nature*, **380**, 416-419.

Liu, M., D.L.Westphal, and T.Holt, 2000: Numerical study of a low-level jet over complex terrain in southern Iran, *Mon. Wea.Rev.*, **128**, 1309-1327.

Nakajima, T., T.Hayasaka, A.Higurashi, G.Hashida, N.Moharram-Nejad, Y.Najafi, and H.Valavi, 1996: Aerosol optical properties in the Iranian region obtained by ground-based solar measurements in the summer of 1991, *J.Appl.Met.*, **35**, 1265-1278.

McClain, C. R., and G. Fargion, 1999: *SIMBIOS Project 1999 Annual Report*, NASA Tech.

Memo. 1999-209486, NASA Goddard Space Flight Center, Greenbelt, Maryland, 128 pp.

Miller, R.L., and I.Tegen, 1998: Climate response to soil dust aerosols, *J.Climate*, **11**, 3247-3267.

O'Neill, N.T., T.F.Eck, B.N.Holben, A.Smirnov, O.Dubovik, and A.Royer, 2001: Uni and bi-modal size distribution influences on the variation of Angstrom derivatives in spectral and optical depth space, *J. Geophys. Res.* (accepted, in press).

Otterman, J., R.S.Fraser, and O.P.Bahethi, 1982: Characterization of tropospheric desert aerosols at solar wavelengths by multispectral radiometry from Landsat, *J.Geophys.Res.*, **87**, 1270-1278.

Peterson, J.T., E.C.Flowers, G.J.Berri, C.L.Reynolds, and J.H.Rudisill, 1981: Atmospheric turbidity over central North Carolina, *J.Appl.Met.*, **20**, 229-241.

Prospero, J.M., 1999: Long-term measurements of the transport of African mineral dust to the southeastern United States: Implications for regional air quality, *J.Geophys.Res.*, **104**, 15,917-15,927.

Reid, J.S., T.F.Eck, S.A.Christopher, P.V.Hobbs, and B.N.Holben, 1999: Use of the Angstrom exponent to estimate the variability of optical and physical properties of aging smoke particles in Brazil, *J.Geophys.Res.*, **104**, 27,473-27,489.

Remer, L.A., Y.J.Kaufman, and B.N.Holben, 1999: Interannual variation of ambient aerosol characteristics on the east coast of the United States, *J.Geophys.Res.*, **104**, 2223-2231.

Schmid, B., J.J.Michaslky, D.W.Slater, J.C.Barnard, R.N.Halthore, J.C.Liljegren, B.N.Holben, T.F.Eck, J.M.Livingston, P.B.Russell, T.Ingold, and I.Slutsker, 2000: Comparison of columnar water vapor measurements during the fall 1997 ARM Intensive Observation Period: solar transmittance methods, *Appl. Opt.*, (submitted).

Schmid, B., J.Michalsky, R.Halthore, M.Beauharnois, L.Harrison, J.Livingston, P.B.Russell, B.N.Holben, T.F.Eck, and A.Smirnov, 1999: Comparison of aerosol optical depth from four solar radiometers during the fall 1997 ARM Intensive Observation Period, *Geophys.Res.Lett.*, **26**, 2725-2728.

Smirnov, A., B.N.Holben, T.F.Eck, O.Dubovik, and I.Slutsker, 2000: Cloud screening and quality control algorithms for the AERONET data base, *Rem. Sens. Env.*, **73(3)**, 337-349.

Sokolik, I.N., and O.B.Toon, 1999: Incorporation of mineralogical composition into models of the radiative properties of mineral aerosol from UV to IR wavelengths, *J.Geophys.Res.*, **104**, 9423-9444.

Tanre, D., Y.J.Kaufman, B.N.Holben, B.Chatenet, A.Karnieli, F.Lavenu, L.Blarel, O.Dubovik, L.A.Remer, and A.Smirnov, 2001: Climatology of dust aerosol size distribution and optical properties derived from remotely sensed data in the solar spectrum, *J.Geophys.Res.* (accepted, in press).

Villevaude, Y.V., A.V.Smirnov, N.T.O'Neill, S.P. Smyshlyaev, and V.V.Yakovlev, 1994: Measurement of aerosol optical depth in the Pacific Ocean and the North Atlantic, *J.Geophys.Res.*, **99**, 20,983-20,988.

Whitby, K.T., 1978: The physical characteristics of sulfur aerosols, *Atm.Env.*, **12**, 135-159.

Figure captions.

Figure 1. Map of the Persian Gulf.

Figure 2. Mean monthly values of aerosol optical depth at the wavelength 500 nm (a), Angstrom parameter (b), and water vapor content (c) (the bars indicate plus or minus one standard deviation).

Figure 3. Mean daily values of aerosol optical depth at the wavelength 500 nm (a), Angstrom parameter (b), and water vapor content (c) for the whole period of measurements.

Figure 4. Frequency of occurrences of aerosol optical depth (a), Angstrom parameter (b), and water vapor content (c).

Figure 5. Seasonal frequency of occurrences of aerosol optical depth, Angstrom parameter and water vapor content. The sum of frequencies is equal to 100% for each season.

Figure 6. Scattergrams of Angstrom parameter versus aerosol optical depth (a), aerosol optical depth versus water vapor content (b) and Angstrom parameter versus water vapor content (c). The two types of symbols in Figure 6b correspond to a partitioning of points into dust (gridded squares) and dust-free (solid circles) classes.

Figure 7. Seasonal diurnal variability of aerosol optical depth at the wavelength 500 nm (solid circles), Angstrom parameter (solid squares), and water vapor content (gridded squares), computed hourly as percent departure from daily average.

Figure 8. Seasonal hourly averages of aerosol optical depth at the wavelength 500 nm (solid circles), Angstrom parameter (solid squares), and water vapor content (gridded squares).

Figure 9. Seasonal aerosol volume size distributions in the total atmospheric column.

Figure 10. Mean monthly aerosol volume size distributions in the total atmospheric column (N is the number of averaged retrievals).

Figure 11. Mean monthly spectral values of the retrieved single-scattering albedo.

Figure 12. Comparison of Angstrom parameters derived from the sunphotometer (solid circles) and nephelometer (dots) measurements.

Table 1. Parameters of aerosol volume size distributions

	Fine mode				Coarse mode			
	C_V	$R_V, \mu\text{m}$	$R_{\text{eff}}, \mu\text{m}$	σ	C_V	$R_V, \mu\text{m}$	$R_{\text{eff}}, \mu\text{m}$	σ
Jun-Sep	0.036	0.16	0.15	0.40	0.226	2.79	2.12	0.74
Oct-Nov	0.035	0.15	0.14	0.37	0.071	2.66	2.13	0.67
Dec-Mar	0.040	0.14	0.13	0.42	0.087	2.27	1.77	0.70
Apr	0.034	0.14	0.13	0.42	0.173	2.33	1.62	0.85
May	0.035	0.10	0.09	0.54	0.221	2.28	1.76	0.72
Aug-98	0.042	0.18	0.17	0.30	0.164	2.98	2.28	0.73
Sep-98	0.037	0.16	0.15	0.30	0.147	2.61	2.04	0.70
Oct-98	0.037	0.15	0.15	0.34	0.078	2.78	2.20	0.69
Nov-98	0.040	0.15	0.14	0.36	0.067	2.70	2.16	0.67
Dec-98	0.037	0.15	0.14	0.40	0.055	2.70	2.11	0.70
Jan-99	0.046	0.16	0.14	0.43	0.058	2.52	1.84	0.79
Feb-99	0.043	0.14	0.13	0.34	0.092	2.39	1.78	0.77
Mar-99	0.040	0.11	0.10	0.35	0.165	2.02	1.65	0.64
Apr-99	0.034	0.14	0.13	0.42	0.173	2.33	1.62	0.85
May-99	0.035	0.10	0.09	0.54	0.221	2.28	1.76	0.72
Jun-99	0.027	0.14	0.11	0.59	0.199	2.72	2.02	0.77
Jul-99	0.036	0.15	0.13	0.53	0.373	2.79	2.12	0.74
mean	0.038	0.14	0.13	0.41	0.149	2.57	1.97	0.73
s.d.	0.005	0.02	0.02	0.10	0.091	0.27	0.22	0.06
var. coef	0.130	0.15	0.17	0.24	0.609	0.10	0.11	0.08

C_V is the volume concentration ($\mu\text{m}^3/\mu\text{m}^2$), R_V is the volume geometric mean radius, R_{eff} is the effective radius, σ is the geometric standard deviation.

Figure 1.

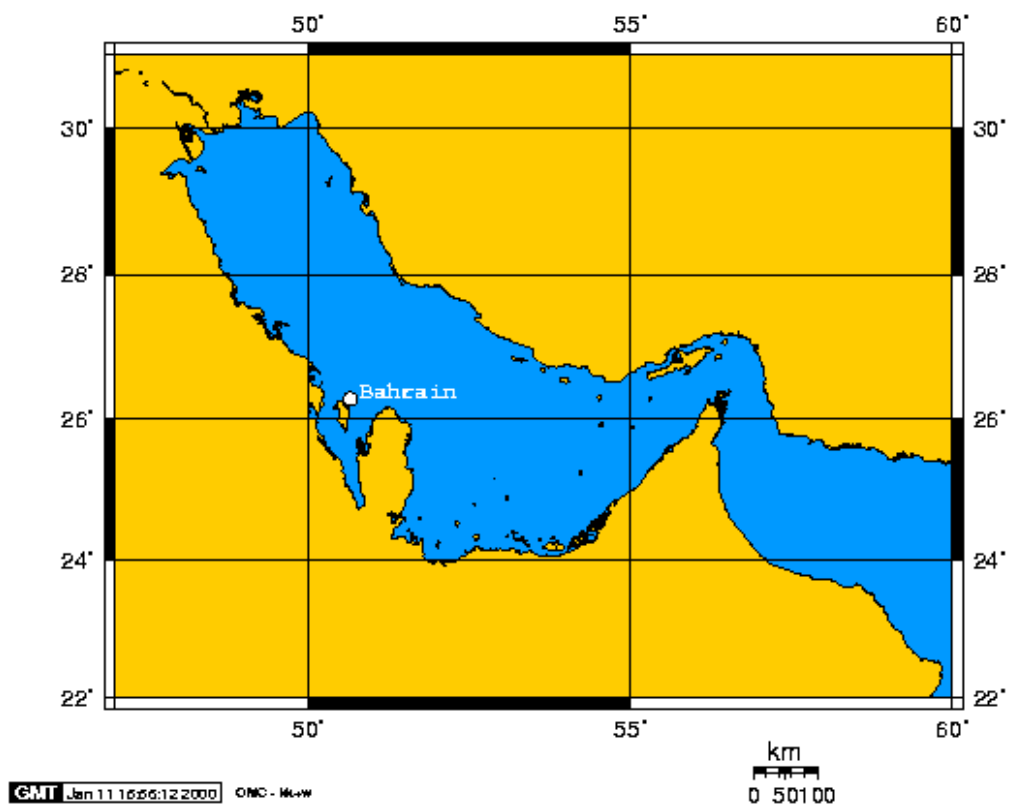


Figure 2

Bahrain

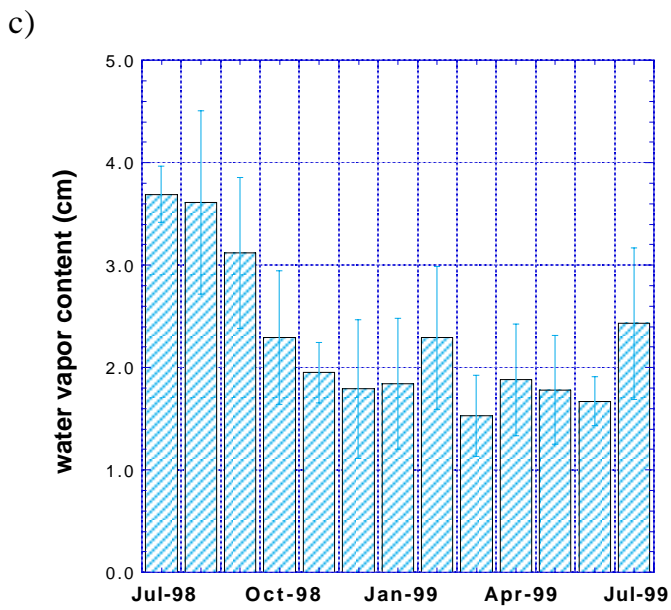
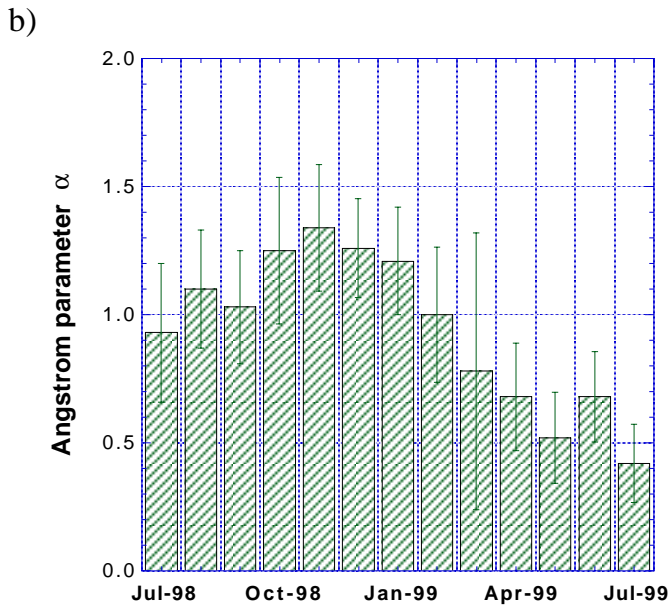
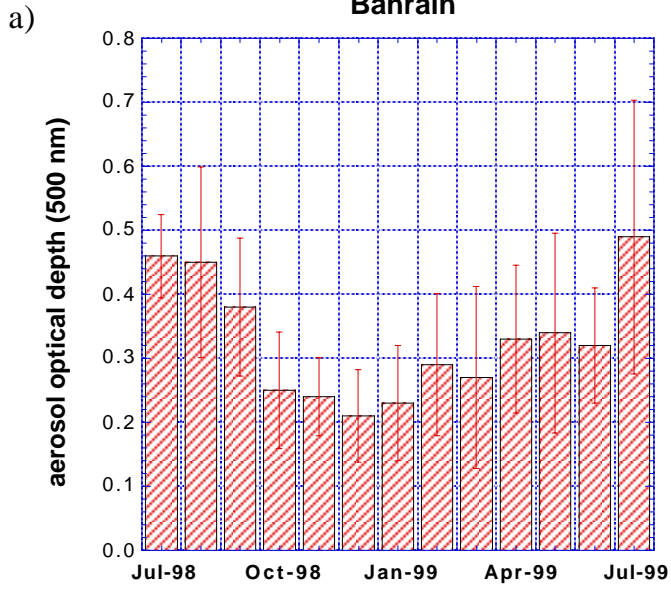


Figure 3

Bahrain

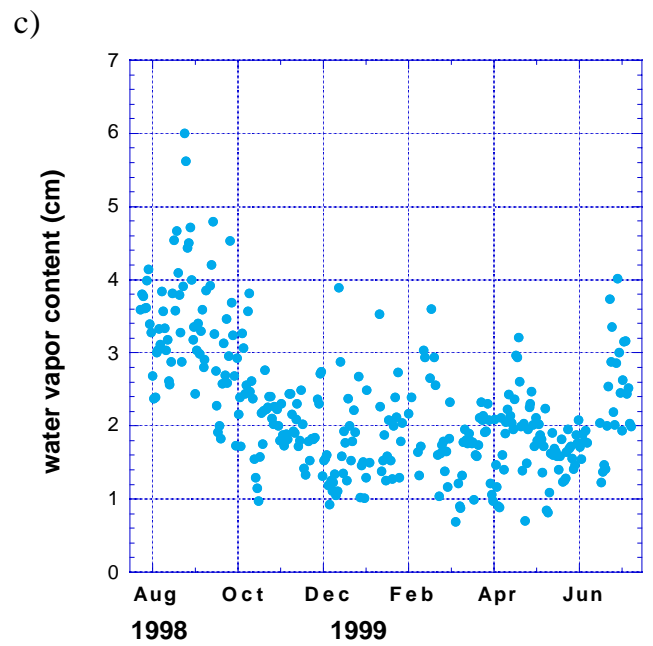
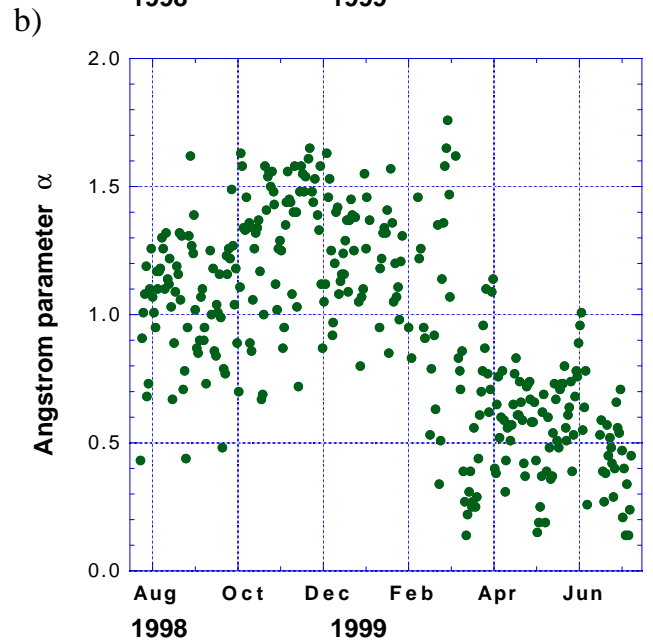
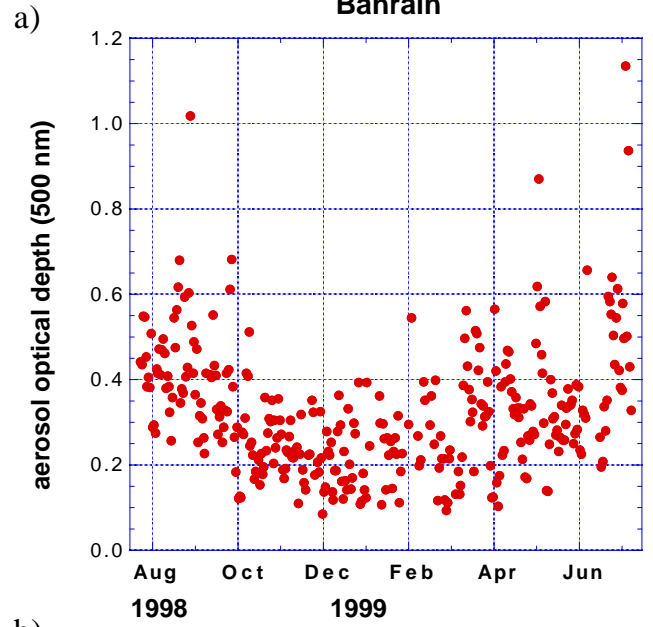
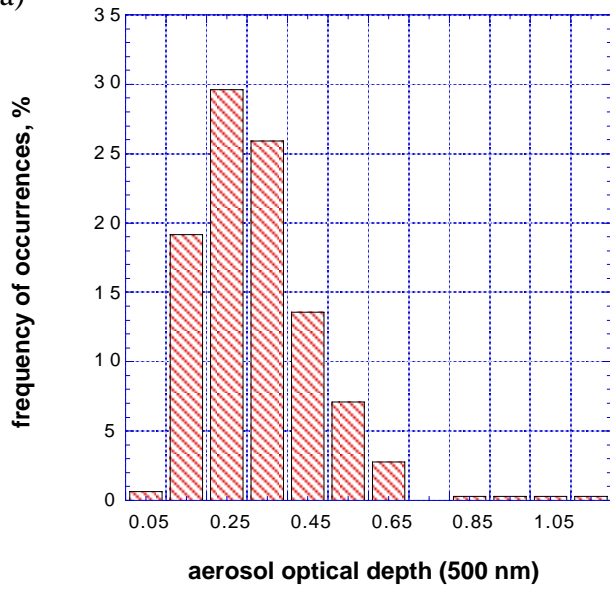


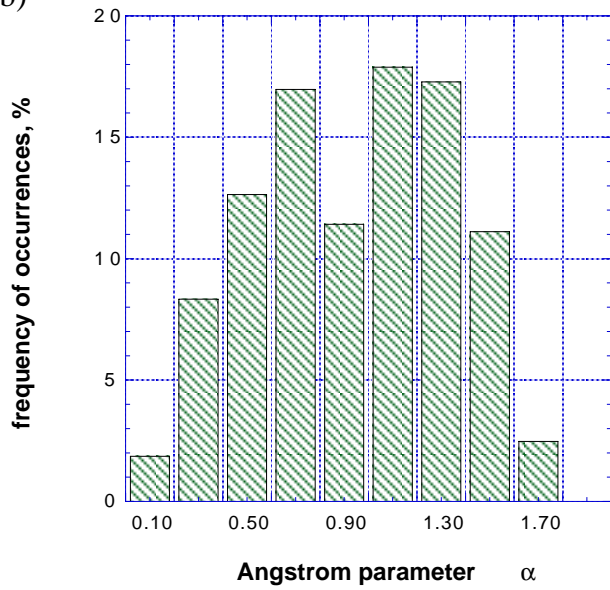
Figure 4

Bahrain

a)



b)



c)

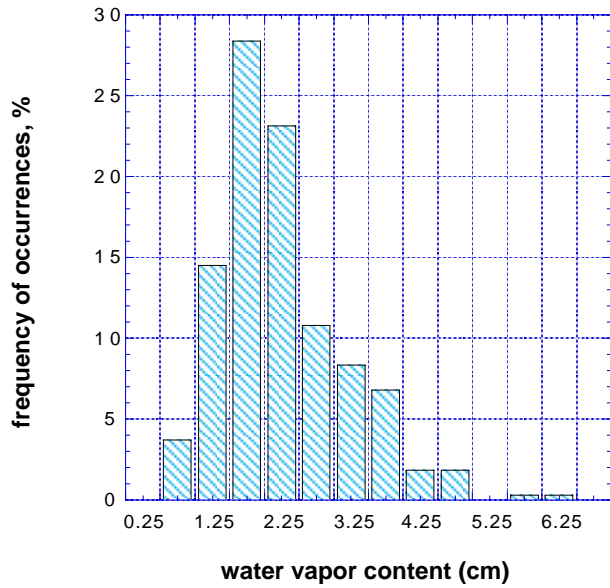


Figure 5

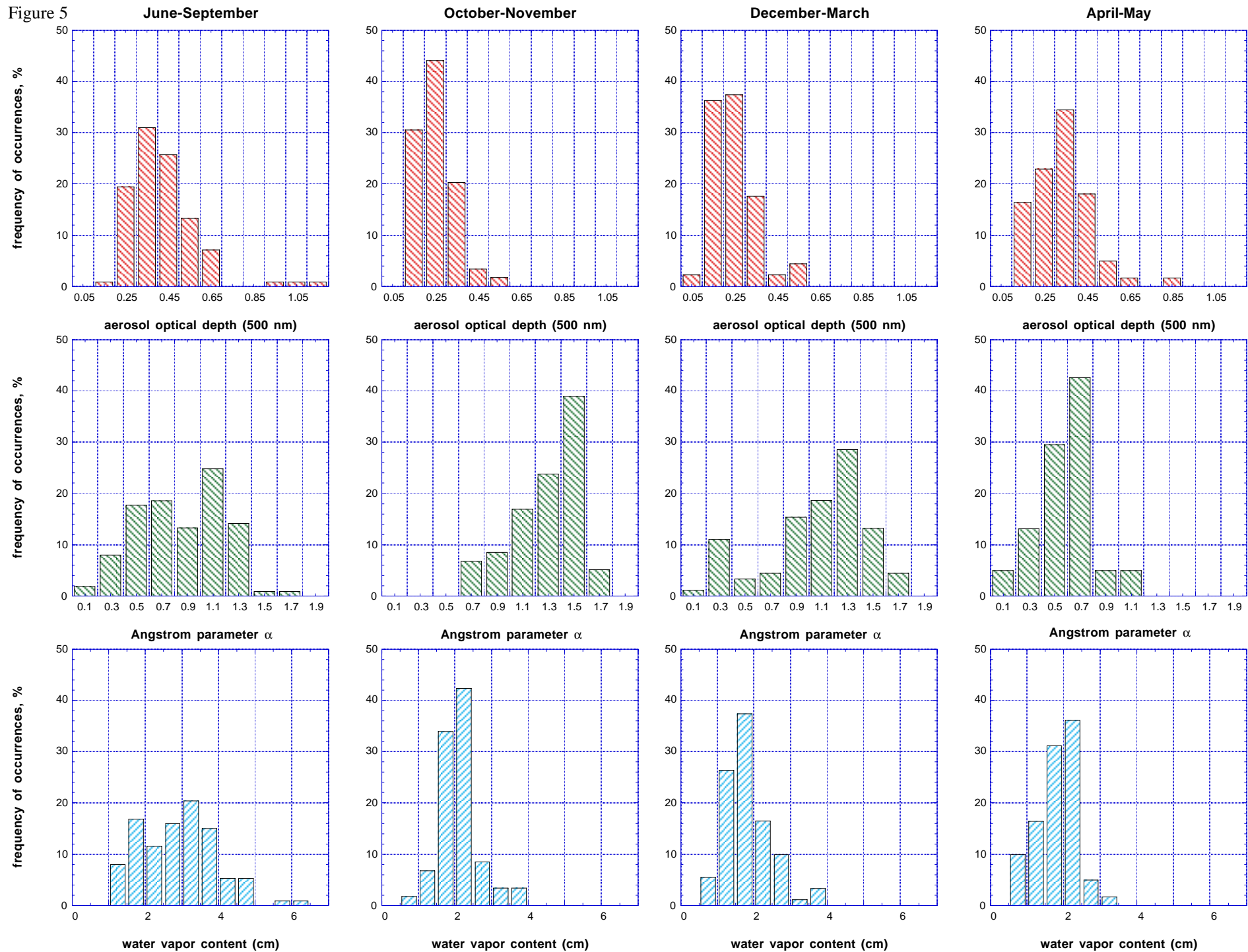
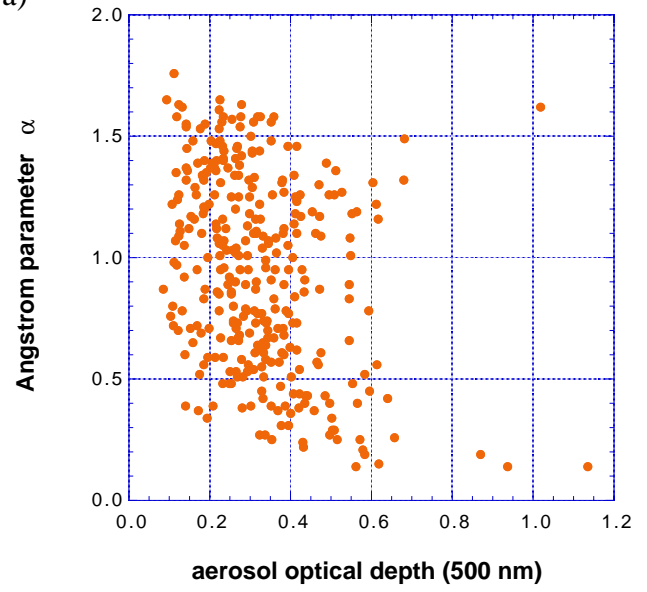


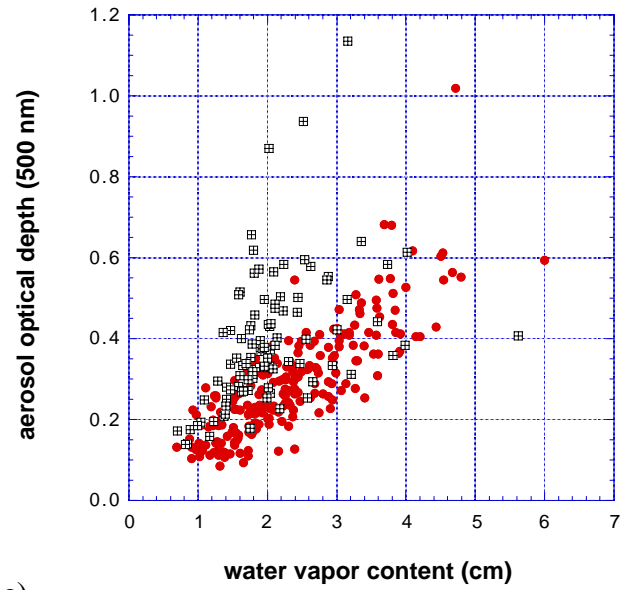
Figure 6

Bahrain

a)



b)



c)

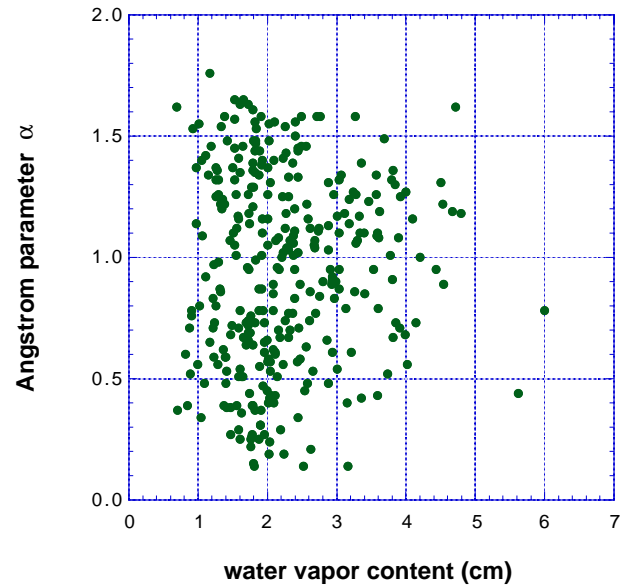


Figure 7

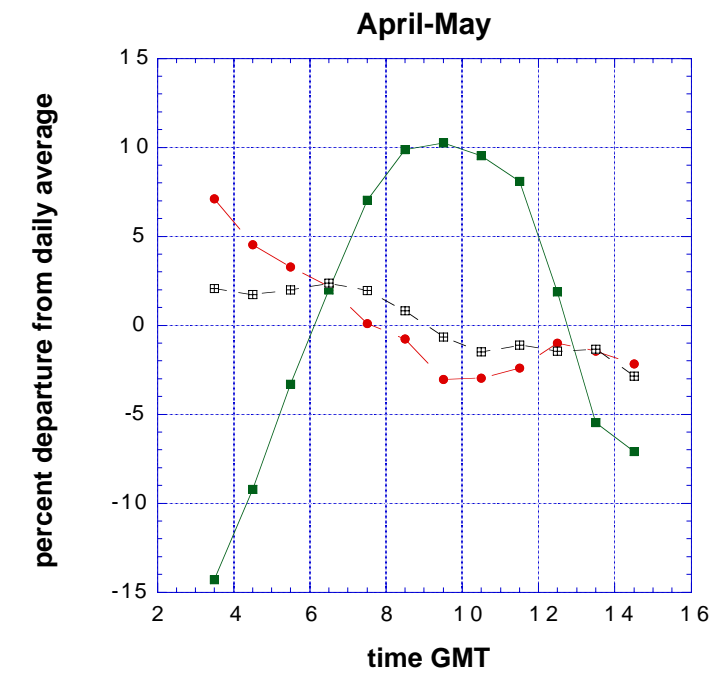
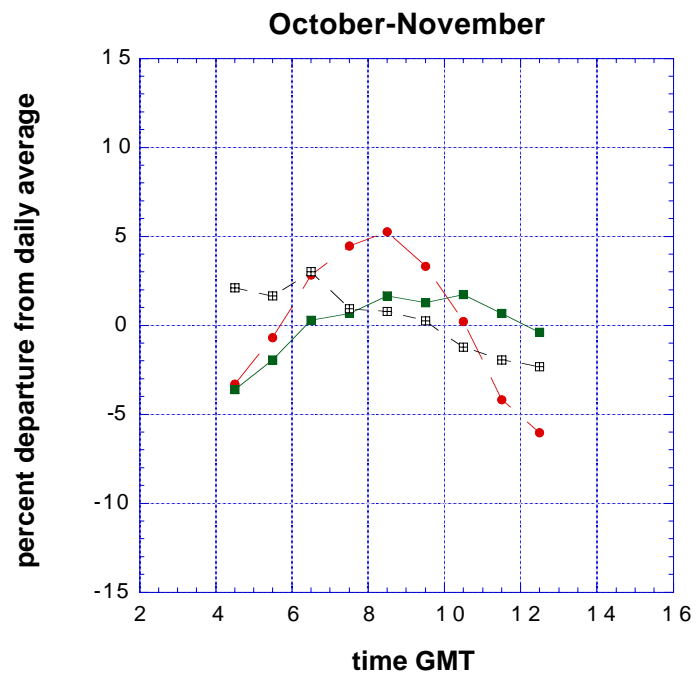
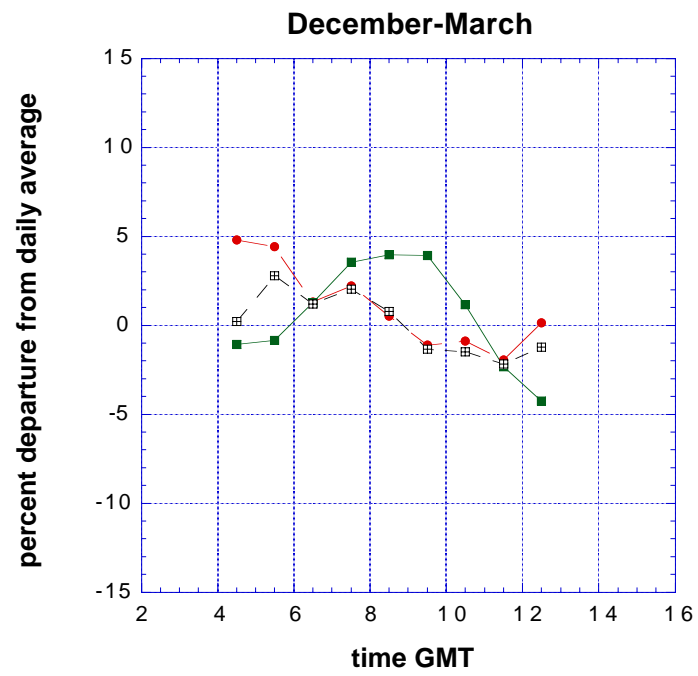
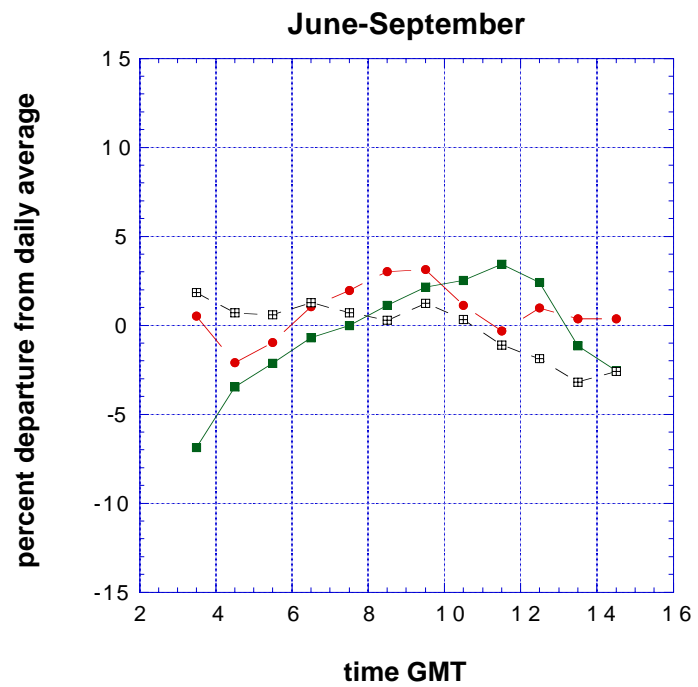


Figure 8

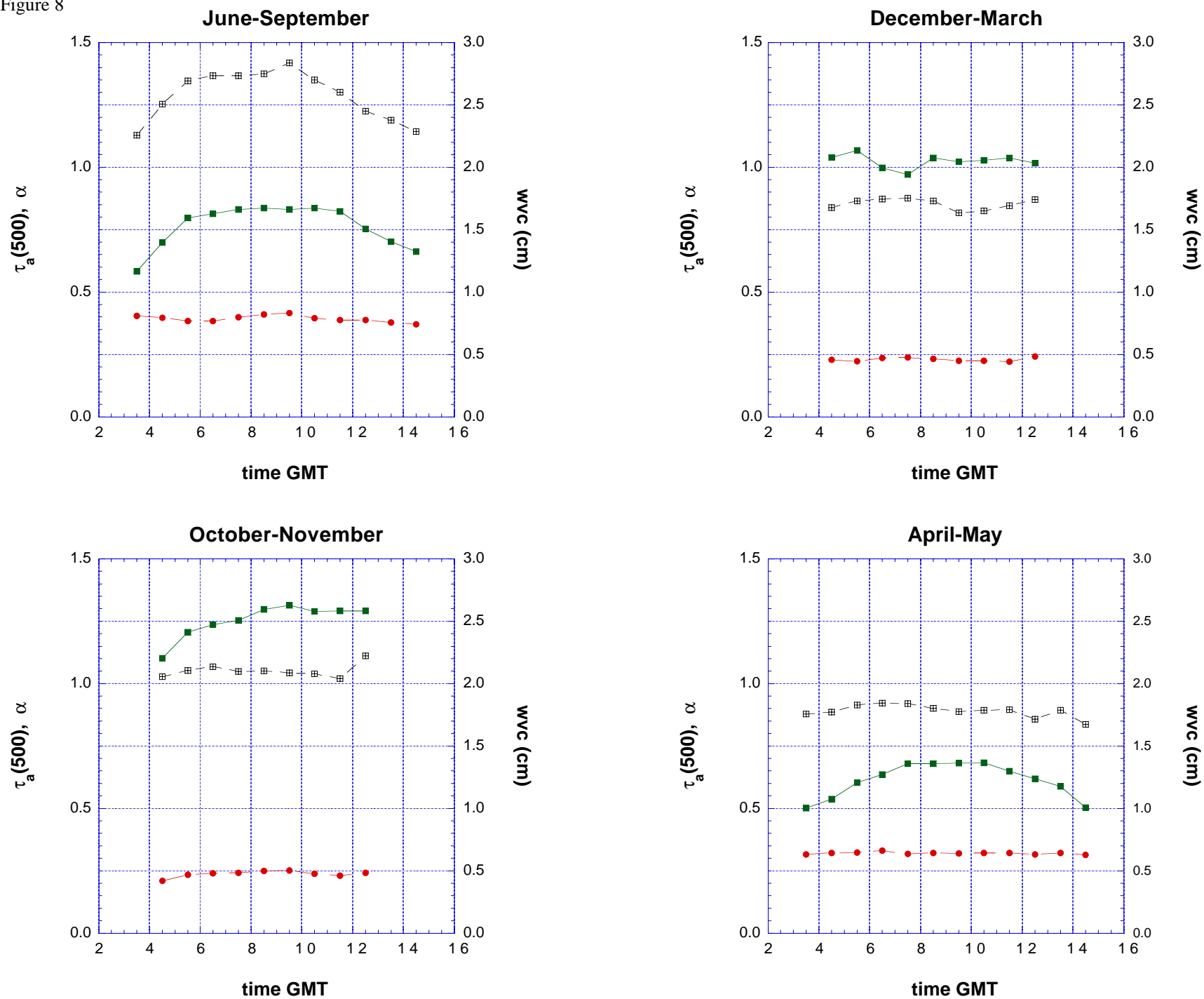


Figure 9

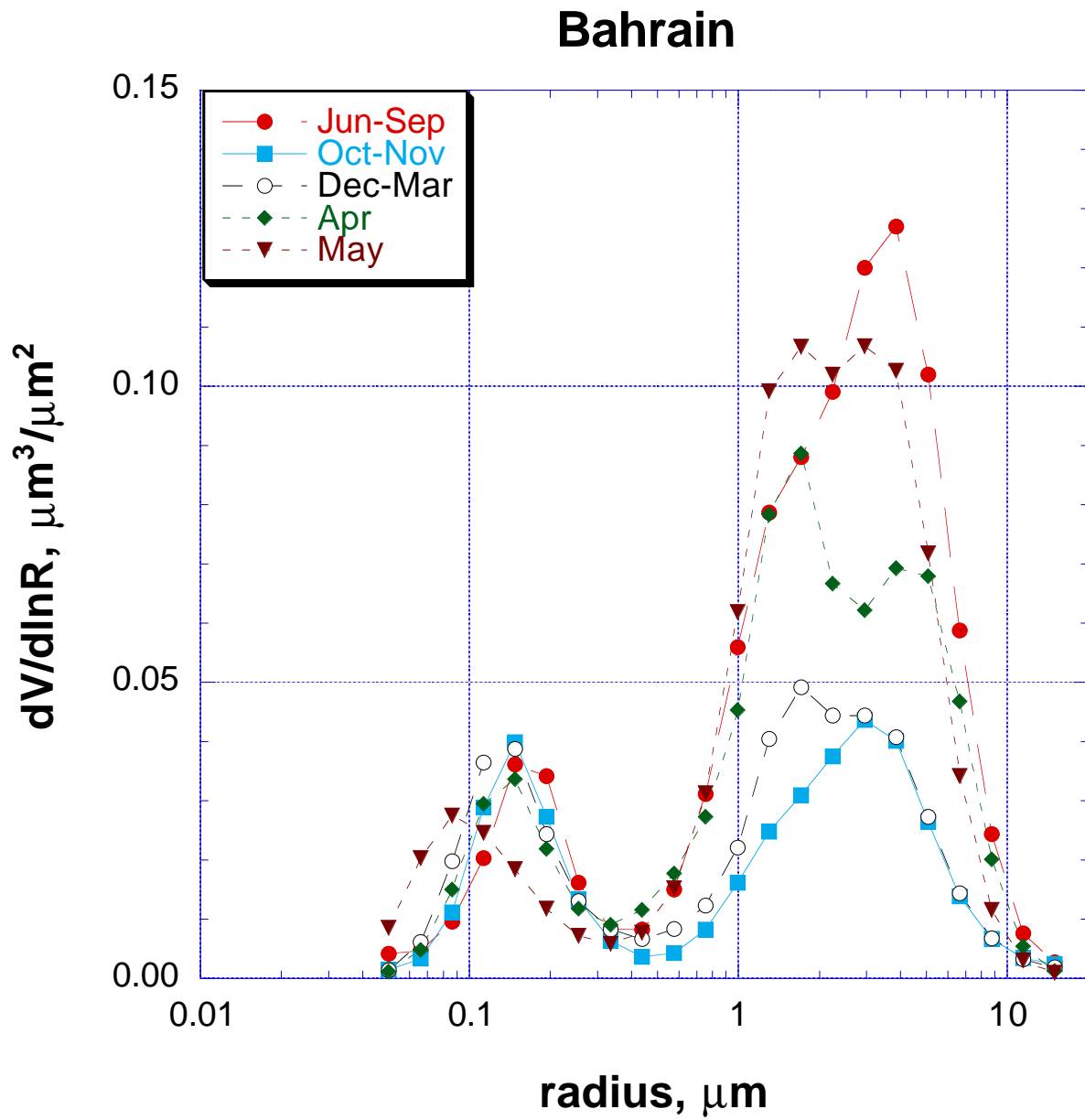


Figure 10

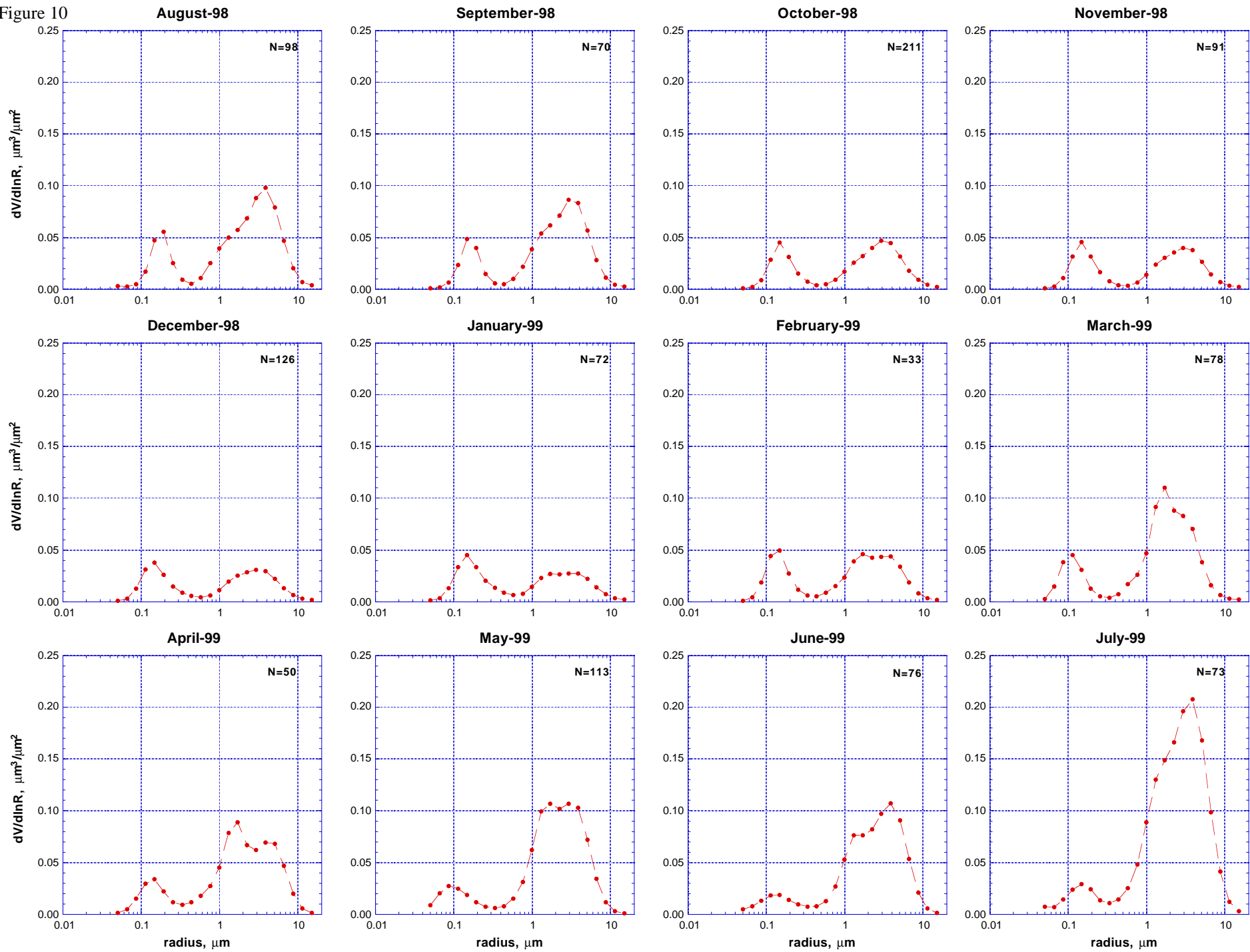


Figure 11

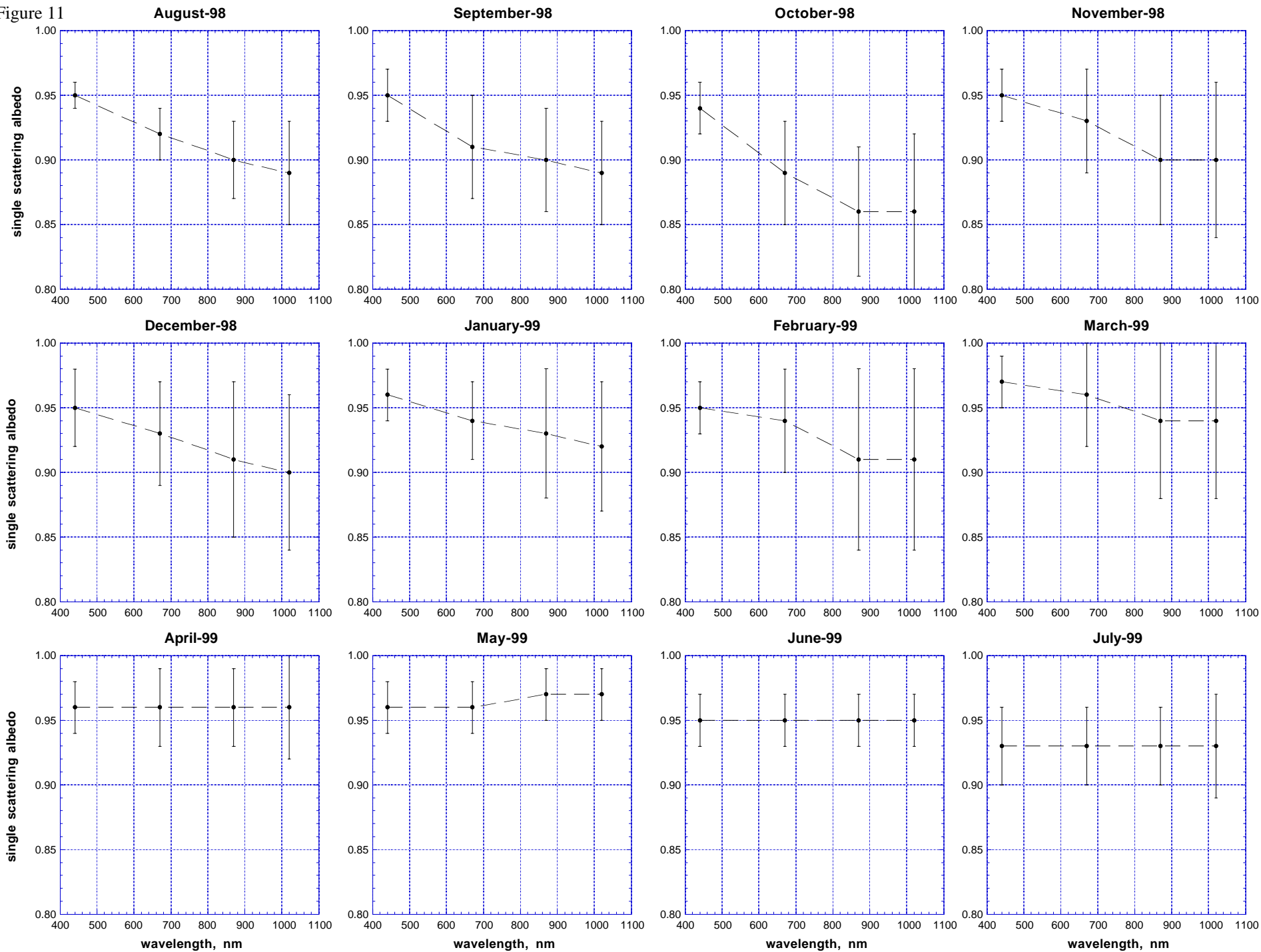


Figure 12

